Materials Science & Engineering A 853 (2022) 143796

Contents lists available at ScienceDirect

Materials Science & Engineering A

journal homepage: www.elsevier.com/locate/msea

Research on plasma arc additive manufacturing of Inconel 625 Ni–Cu functionally graded materials

Yanhu Wang [a,b], Sergey Konovalov [a,b], Xizhang Chen [a,b,*], R. Arvind Singh [a], S. Jayalakshmi [a]

[a] Zhejiang Provincial Key Laboratory of Laser Processing Robotics, College of Mechanical and Electrical Engineering, Wenzhou University, Wenzhou, 325035, Zhejiang, China

[b] Siberian State Industrial University, 42, Kirova Str, Novokuznetsk, 654007, Russia

ARTICLE INFO

Keywords:
Additive manufacturing
Functionally graded materials
Mechanical properties
Corrosion

ABSTRACT

In this work, a plasma arc additive manufacturing technique with a double-wire feedback mechanism was used to manufacture Inconel 625 Ni–Cu functionally graded materials. The microstructure, mechanical properties and corrosion properties of the deposited alloy were evaluated. Microstructure observation and tensile testing of parts with different element contents indicated that functionally graded materials were obtained through the manufacturing process. The results have shown that due to the very high growth restriction factor Q of Cu, its addition can increase the constitutional supercooling zone, resulting in a decrease in columnar and dendrites and an increase in equiaxed crystals in the Inconel 625 Ni–Cu functionally graded material, as well as changing the Schmid factor (SF) distribution. The tensile strength and ductility of the Inconel 625 Ni–Cu functionally graded materials increased with increasing Cu content, while the corrosion resistance of the alloy decreased with increasing Cu content during electrochemical corrosion tests.

1. Introduction

Functionally graded materials (FGMs) are a new type of composite material in which two or more materials are combined with continuous gradient changes in composition and structure, resulting in a gradual change in properties and functions. Its design requires that the function and performance vary with the change in the internal position of the component, and this can be satisfied by optimizing the overall performance of the component. FGMs were proposed by Noda [1] based on observations of naturally grown materials and structures, such as bone, wood and teeth, which consist of graded structures and exhibit properties that surpass those of the individual component materials [2–6]. FGMs can be classified into two major categories. From the perspective of material combinations, FGMs can be divided into metal/alloy, metal/nonmetal, metal (nonmetal)/ceramic and other combinations, so a variety of materials with special functions can be obtained. From the perspective of the change in material composition, FGMs can be divided into (1) functionally graded coating types, that is, coatings with gradual compositions formed on the base material. (2) The gradient functional connection type, that is, the composition of the seam bonded between the two substrates, changes in a gradient. (3) Gradient functional integral type, that is, a structural material with a gradient of material composition from one side to the other. FGMs have huge application potential in aerospace, biomedical engineering, sensors, and energy areas [7,8].

In terms of the geometry of FGMs, there are two categories of FGMs: thin film/coating and bulk. Currently, the conventional manufacturing methods for thin film/coated FGMs mainly include vapor deposition [9–11] and liquid phase processes [8,12]. Zhang [8] found that vapor deposition has high energy consumption and a long cycle. Yan [13] reported that powder metallurgy cannot produce continuous grading, as powder mixing and stacking should be performed before the final sintering. Additionally, James [14] found that powder metallurgy techniques almost always contain pores that degrade mechanical properties. Mahamood [15] stated that the centrifugal casting method has the potential for mass production, but it can only fabricate cylindrical parts.

All these traditional methods are not suitable to produce complex geometries and often result in pores, which reduces product quality and increases cost. As an emerging technology, additive manufacturing (AM) provides an effective method to solve the drawbacks of traditional methods. It offers the potential for local control of the composition and microstructure and can produce complex FGMs with multidimensional

* Corresponding author. Zhejiang Provincial Key Laboratory of Laser Processing Robotics, College of Mechanical and Electrical Engineering, Wenzhou University, Wenzhou, 325035, Zhejiang, China.
E-mail address: Kernel.chen@gmail.com (X. Chen).

https://doi.org/10.1016/j.msea.2022.143796
Received 27 May 2022; Received in revised form 7 August 2022; Accepted 10 August 2022
Available online 17 August 2022

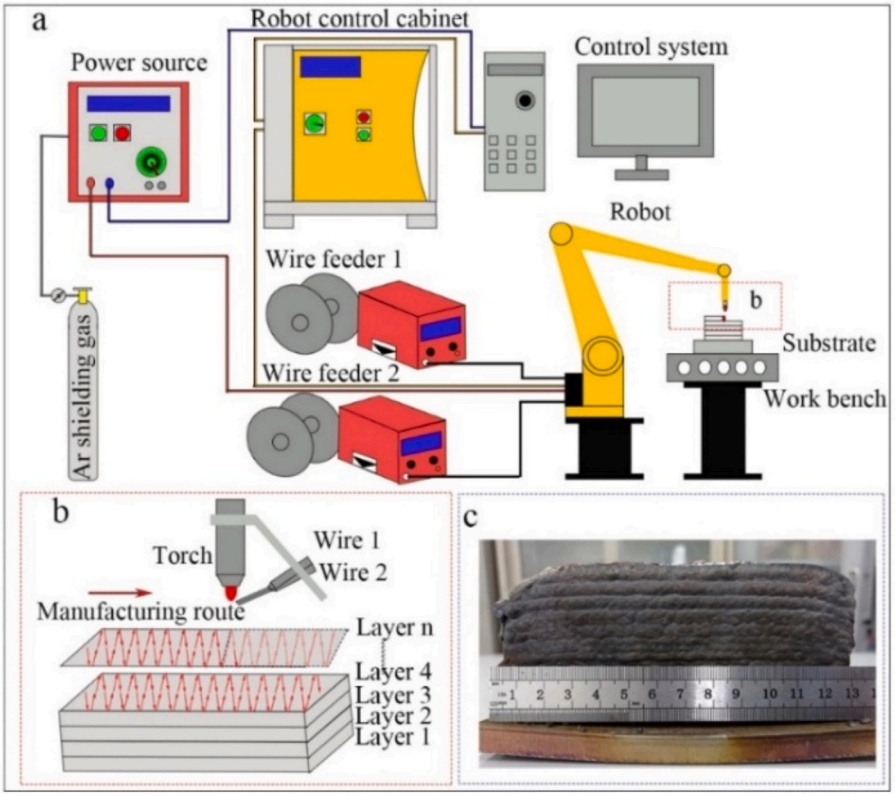

Fig. 1. Illustration of the plasma arc additive manufacturing setup (a), illustration of deposition (b) and as-deposited sample (c).

Table 1
ERNiCrMo-3 wire composition (wt.%).

Element	Cr	Mo	Nb	Fe	Mn	Ti	Al	C	Ni
Content	20–23	8–10	3.15–4.15	≤5	≤0.5	≤0.4	≤0.4	≤0.1	Bal.

Table 2
Process parameters used during plasma arc additive manufacturing of Ni–Cu functionally gradient material alloys.

	Part 1		Part 2		Part 3
parameter	value	unit	value	unit	Value unit
Deposition current	120	A	110	A	100 A
Deposition voltage	10.4	V	10.4	V	10.4 V
ERNiCrMo-3 wire speed	1.5	m/min	1.5	m/min	1.5 m/min
Cu wire speed	0.7	m/min	0.6	m/min	0.5 m/min
Travel speed	0.5	m/min	0.5	m/min	0.5 m/min
Pure argon	20	L/min	20	L/min	20 L/min
Dwell time between deposition layers	60	s	60	s	60 s
Angle between the torch and filler wire	75	°	75	°	75°
Distance between the torch and workpiece	25	mm	25	mm	25 mm

and directional gradient structures. Due to the high energy density of the plasma arc, strong arc directionality, high arc column temperature, and high deposition efficiency, it has become an ideal heat source in arc additive manufacturing [16].

In this research, a plasma arc additive manufacturing technique with a double-wire feedback mechanism was used to manufacture Inconel 625 Ni–Cu functionally graded materials. The Inconel 625 Ni-based superalloy has excellent strength and corrosion resistance. The addition of Cu to the additively manufactured Inconel 625 Ni-based superalloy not only improves the formation of columnar crystals, but also increases its strength and corrosion resistance. Inconel 625 Ni–Cu functionally graded materials were produced. The alloys were analyzed for their (1) effect of their composition on their mechanical properties and (2) their corrosion behavior.

2. Experimental setup

2.1. Process and equipment used for additive manufacturing

An illustration of the plasma arc additive manufacturing setup is shown in Fig. 1a. The deposition process of the Ni–Cu functionally gradient material alloy is shown in Fig. 1b. The deposition was performed by using intelligent plasma remanufacturing system equipment. It is powered by Transmit 550i multifunctional inverter DC power. The welding torch is a PWM-300 plasma welding torch. Two standard welding wires were fed by two ET201 wire feeder machines. One was a 1.2 mm diameter ERNiCrMo-3 wire, and the other was a 1.2 mm diameter 99.9% Cu wire. The two wires were fed into a single molten pool under independent control of the feed rate. The change in alloy content was achieved by controlling the wire feed speed. The elemental composition of the ERNiCrMo-3 wire is given in Table 1. The substrate over which the multilayer deposition was conducted was a steel plate that had dimensions of 150 mm × 50 mm × 10 mm. Pure argon gas was

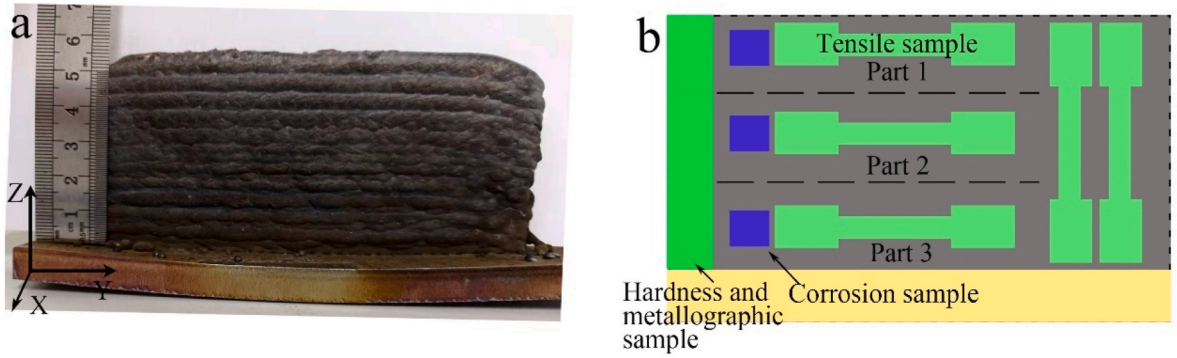

Fig. 2. As-fabricated sample (a) and schematic showing the locations from which samples were taken for different tests (b).

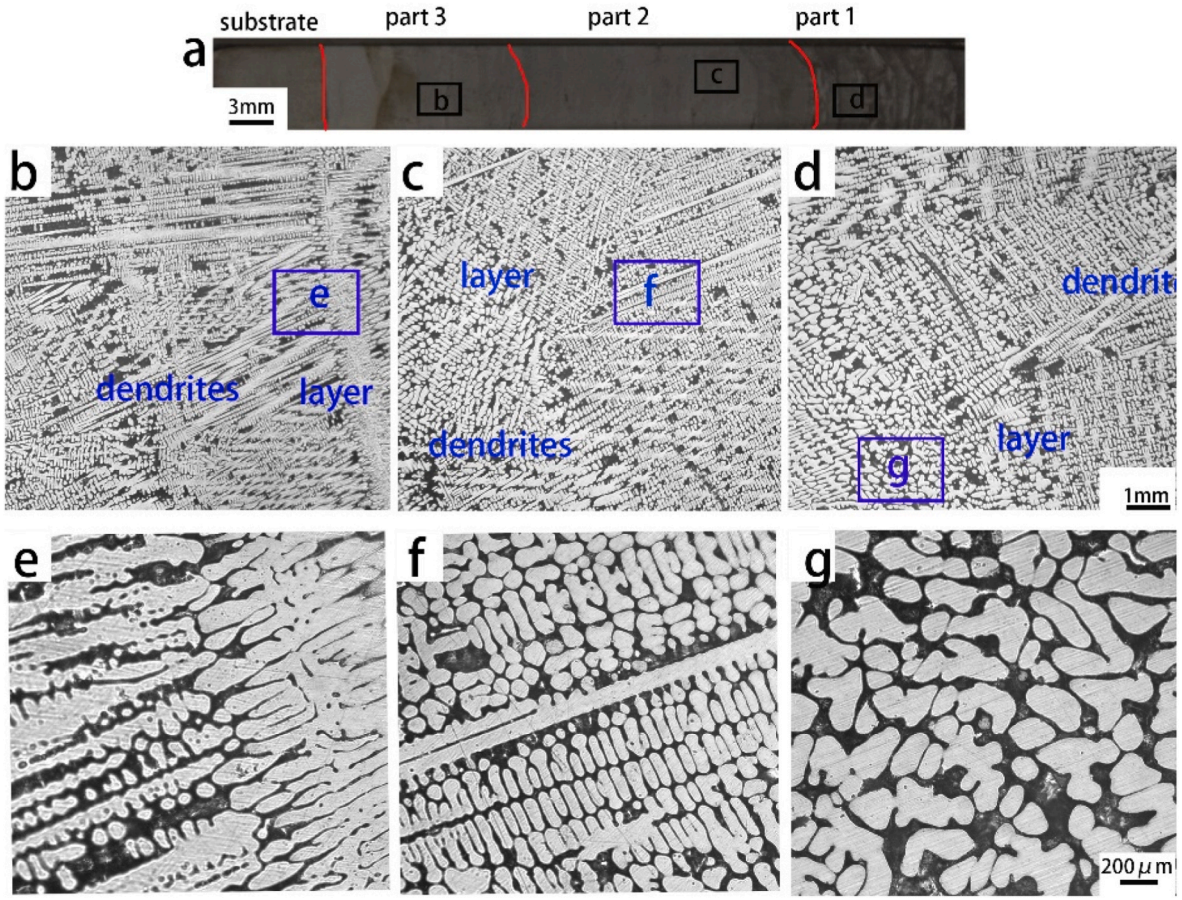

Fig. 3. Optical micrograph of the sample manufactured by WAAM (a) and magnified optical micrographs of the wall at different locations (b–g).

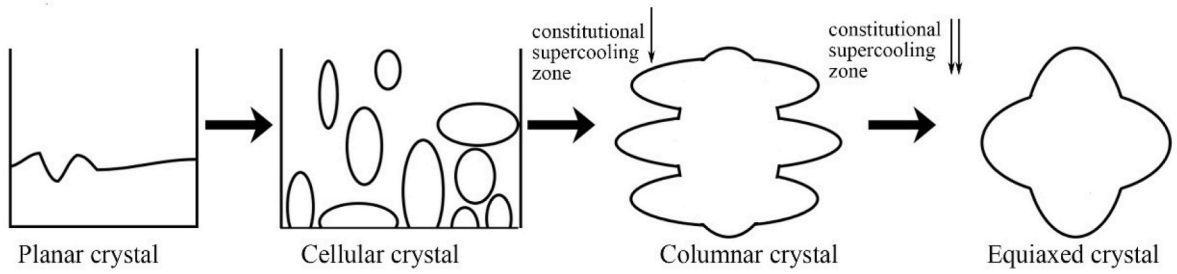

Fig. 4. The microstructure evolution of Inconel 625 Ni–Cu functionally graded materials in plasma arc additive manufacturing.

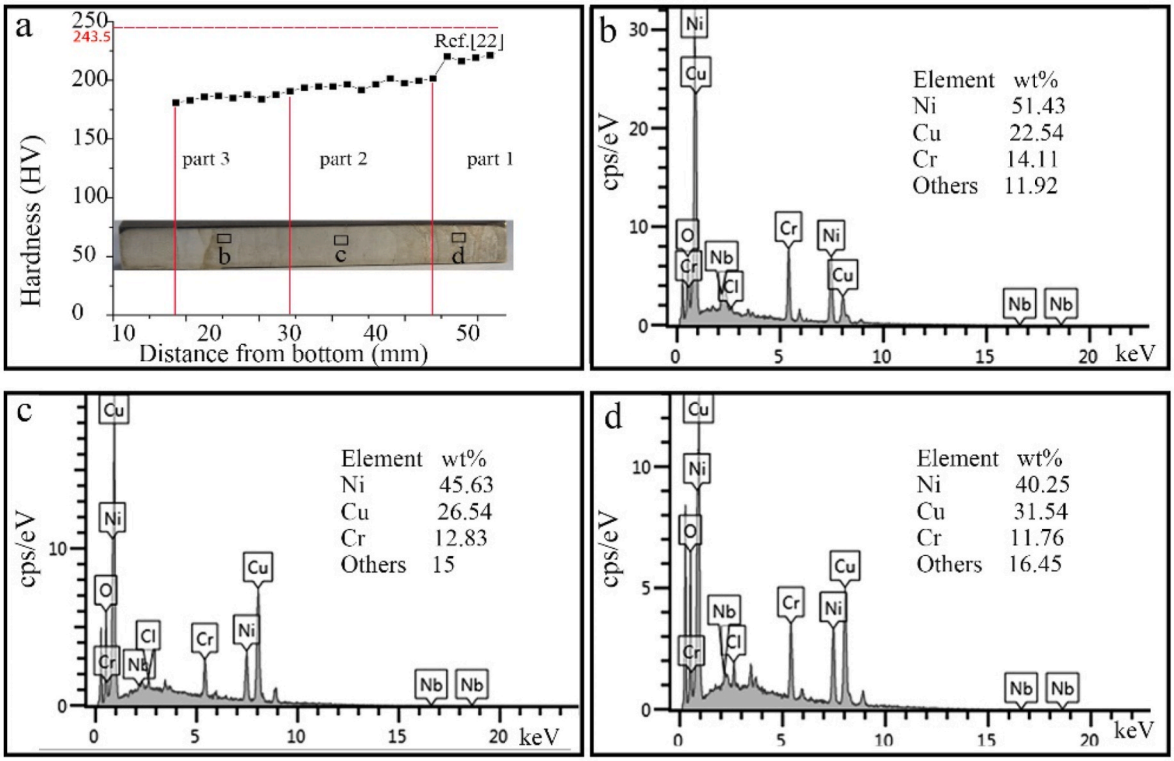

Fig. 5. Hardness (a) and detection area (b–d) of the deposited sample composition is 10x20 mm^2.

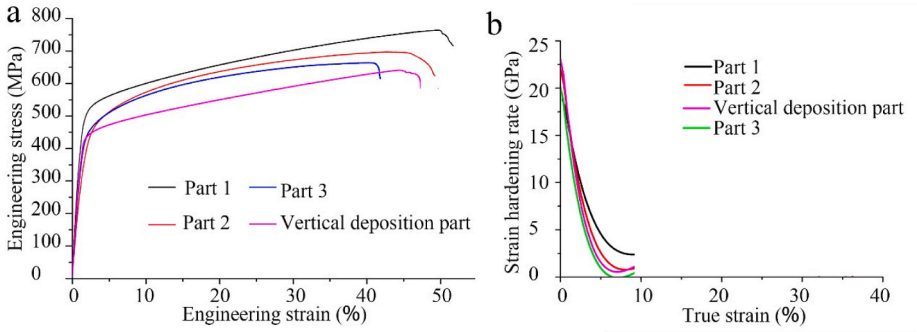

Fig. 6. Tensile stress-strain curves (a) and strain hardening rate curves (b).

Table 3
The yield, tensile strength, and elongation results.

	Yield Strength (MPa)	Tensile Strength (MPa)	Elongation (%)
Part 1	432	721	49
Part 2	419	680	45
Part 3	410	650	42
Vertical deposition layer	408	640	44
Ref. [25]	264	581	33
Ref. [26]	377	650	42

employed for shielding during the plasma arc additive manufacturing process. The trial and error are used to obtain the near-optimal process parameters. The welding process parameters employed for deposition are given in Table 2.

2.2. Testing of the deposited alloy

The deposited Ni–Cu FGMs alloy sample is shown in Fig. 2a. The deposited sample can be divided into three parts (part 1, part 2 and part 3) from the top to the bottom according to the change in copper and nickel content, as shown in Fig. 2b. The microstructure and mechanical properties of the samples were studied. For these studies, test samples were extracted from the fabricated wall, as shown in Fig. 2b. The metallographic samples were prepared per a standard metallographic procedure and etched with aqua regia (15 ml HCl + 5 ml HNO_3). The microhardness values of the alloy were measured by an HV-1000 microhardness tester at a 100 g test load for 15 s. The dimensions (width, thickness, and length) of the tensile samples were 8 × 2 × 40 mm^3. The corrosion test was carried out in a conventional three electrode cell containing 3.5% NaCl solution at room temperature using Vertex. One EIS electrochemical workstation was used, in which the specimen was suspended as a working electrode and the counter electrode was a Pt rod. The surface morphology of the corrosion samples was analyzed using a Dimension Icon atomic force microscope (Dimension

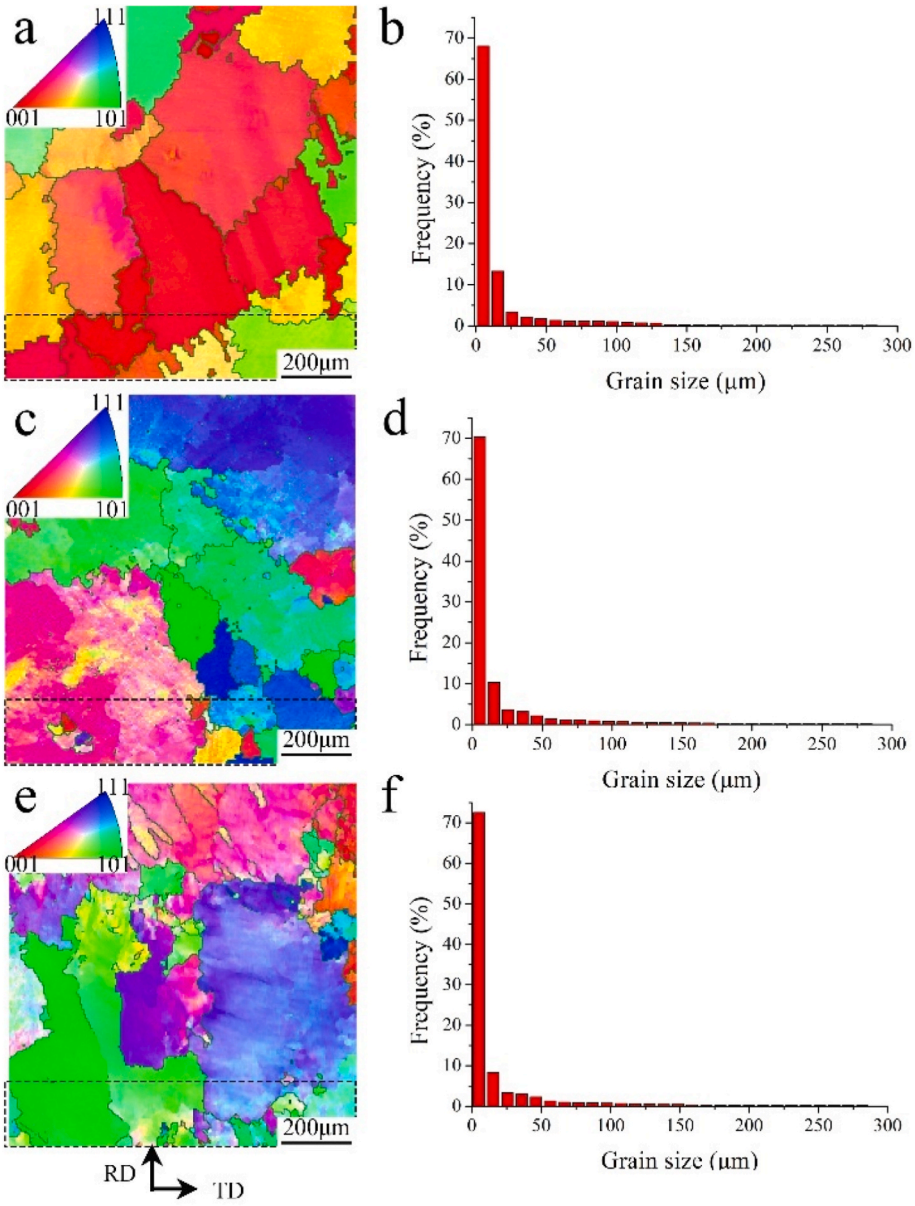

Fig. 7. EBSD inverse pole figures for the microstructure samples (a: part 1, c: part 2, e: part 3) and the grain size distribution (b: part 1, d: part 2, f: part 3).

Icon AFM) and a Phenom XL desktop scanning electron microscope (SEM).

3. Results and discussion

3.1. Microstructure

Fig. 3a shows an optical micrograph of the sample. The deposited sample is fully dense. There are no cracks or porosities in each layer or between two subsequent layers in the sample. The dendrites spread throughout the sample, and most of them grew along the building direction (Fig. 3b–d). There is a mixture of cellular and dendritic grains with very fine secondary arms near the interface (Fig. 3e). There was a long dendrite far away from the interlayer, and small secondary dendrites formed on it (Fig. 3f). Additionally, equiaxed grains are present. There is epitaxial growth of some grains between the layers, as seen in Fig. 3e and f. However, there is a sharp change in the grain structure between the layers, i.e., at the interface, most of them are cellular grains, as shown in Fig. 3g.

It is observed that the microstructure of the deposited alloy is a mix of equiaxed grains, columnar grains, and dendrites (Fig. 3b–g). From part 3 to part 1, the crystal grains become finer. As the sample was made layer by layer, the solidification microstructure and the grain size depended strongly on the location of the deposited layer of the sample, solidification rate (R), temperature gradient (G), and melt composition [17,18]. According to the work of Wang [19], columnar grains are mostly found in samples made by wire arc additive manufacturing (WAAM). The orientation of grain growth is largely governed by the direction of heat flux. Wang [20] found that there will be a temperature gradient in the multi-pass process, and the heat flux provides the driving force for columnar grain and dendrites growth.

The microstructure evolution of Inconel 625 Ni–Cu functionally graded materials in plasma arc additive manufacturing is shown in Fig. 4. Since Cu has a very high growth restriction factor Q, according to the interdependence theory, constitutional supercooling zone is critical to the grain size [21]. The larger the constitutional supercooling zone, the finer the grains. However, the rate of development of the constitutional supercooling zone is controlled by the Q. Larger values of Q

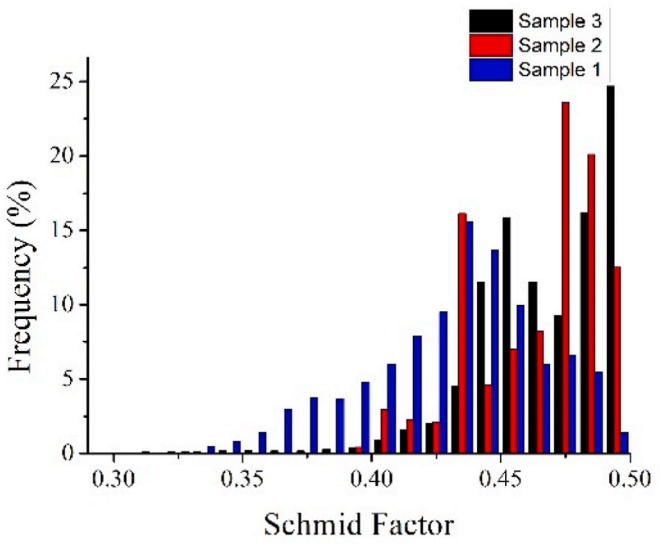

Fig. 8. SF distribution of the samples.

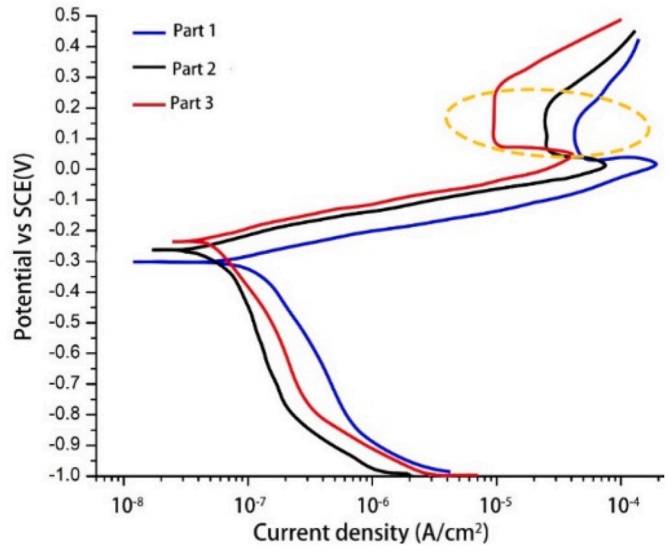

Fig. 9. Potentiodynamic polarization curves.

Table 4
Corrosion data of part 1, part 2 and part 3.

	E_{corr} (mV)	E_{pit} (mV)	I_{corr} (μA/cm^2)
Part 1	−300	218	0.124
Part 2	−235	242	0.058
Part 3	−198	285	0.049
Ref. [31]	−264	600	0.470
Ref. [32]	−273	472	0.220

promote more nucleation. Since the Cu content is reduced from part 1 to part 3, the constitutional supercooling zone is also reduced, resulting in a decrease in columnar crystals and dendrites and an increase in equiaxed grain in the part 1.

3.2. Hardness and element content

The hardness values from the bottom to the top of the fabricated sample are shown in Fig. 5a. To detect the content of the sample, the middle positions of the three parts (as shown by the square marks in Fig. 5a) were selected for surface scanning, and the element content results are shown in Fig. 5b–d. From part 1 to part 3, the content of Cu decreases, while the contents of Ni and Cr increase. The other elements are mainly Nb, Cl and O.

The hardness values range from 179 to 230 Hv. The hardness is significantly lower than that of the wire arc additive manufactured Inconel 625 alloy (243.5 HV) [22]. The hardness decreases from part 3 to part 1. This may be due to the effect of Ni reducing the hardenability, and the high Q of Cu helps to refine the grain structure. From the microstructure analysis, the large columnar crystals and dendrites from part 3 to part 1 gradually decreased, while the small equiaxed crystals increased. According to the Hall-Petch relation, as the grain size decreases, the hardness of the alloy increases [23].

3.3. Tensile properties

The tensile properties of the samples in part 1, part 2, part 3 and the vertical deposition part are studied, the corresponding tensile curves and strain hardening rate curves are shown in Fig. 6, and the tensile results are shown in Table 3. The yield strength, tensile strength and elongation of part 1 are higher than those of part 2. Part 2 is higher than part 3. The yield strength and tensile strength of the vertical deposition part are lower than those of sample 3. While the elongation is higher than that of sample 3. It can be known from the strain hardening rate curves that although the strain hardening rate of these four parts does not change significantly, the rate of decrease of the strain hardening rate of each part varies with the increase of plastic deformation. (part 1 < part 2 < vertical deposition part < part 3). The slow change of strain hardening rate indicates that the ability to resist plastic deformation is strong, and the plasticity (ductility) is better, so it can be shown that part 1 has the best ductility.

The difference in performance of the three parts is mainly related to the change in Cu and Ni content in the alloy. On the other hand, as Ni is stiffer and has a smaller lattice constant than Cu, as the Cu content increases, the stiffer lattice becomes weak, making it easier for grains to deform and rotate past each other, increasing the strength. On the other hand, since high-Q copper affects the growth of grains, with the increase of copper content, the constitutional supercooling zone also increases, and the growth of columnar grain and dendrites is limited, resulting in the formation of more equiaxed and fine grains, thereby increasing the strength.

While the performance in the vertical direction is lower than those of these three parts. Due to the inherent properties of additive manufacturing (the sample was made layer by layer), the solidification microstructure and the grain size depended strongly on the location of the deposited layer of the sample. Therefore, the grains grow along the deposition direction (vertical direction), and it is easy to form columnar crystals and reduce the performance. The grains in the horizontal direction are relatively uniform. The inhomogeneity of grain structure leads to lower load-bearing capacity of the samples taken from the vertical direction (as in the vertical direction, significant interlayer transition zone exists). It may also be affected by the change in texture orientation of the samples [24]. The performance is better than that of the Inconel 625 sample prepared by sand casting [25] and WAAM based on cold metal transfer [26]. The improvement of performance is mainly based on the addition of Cu to refine the grains, reduce the columnar and dendrites, and increase the equiaxed grains. Through the comparison of tensile properties, it can be found that changing the copper content can change the properties of the alloy. Functionally graded materials can be prepared using this method.

The specimens of Electron backscattered diffraction (EBSD) are cut from the uniform deformation regions close to the fracture surface and along the direction parallel to tensile axis. EBSD inverse pole figure (IPF) of the samples indicate that microstructure with randomly oriented and equiaxed grains are available as shown in Fig. 7a, c and e. However, they have a clear trend with many subdrains in the region near the bottom

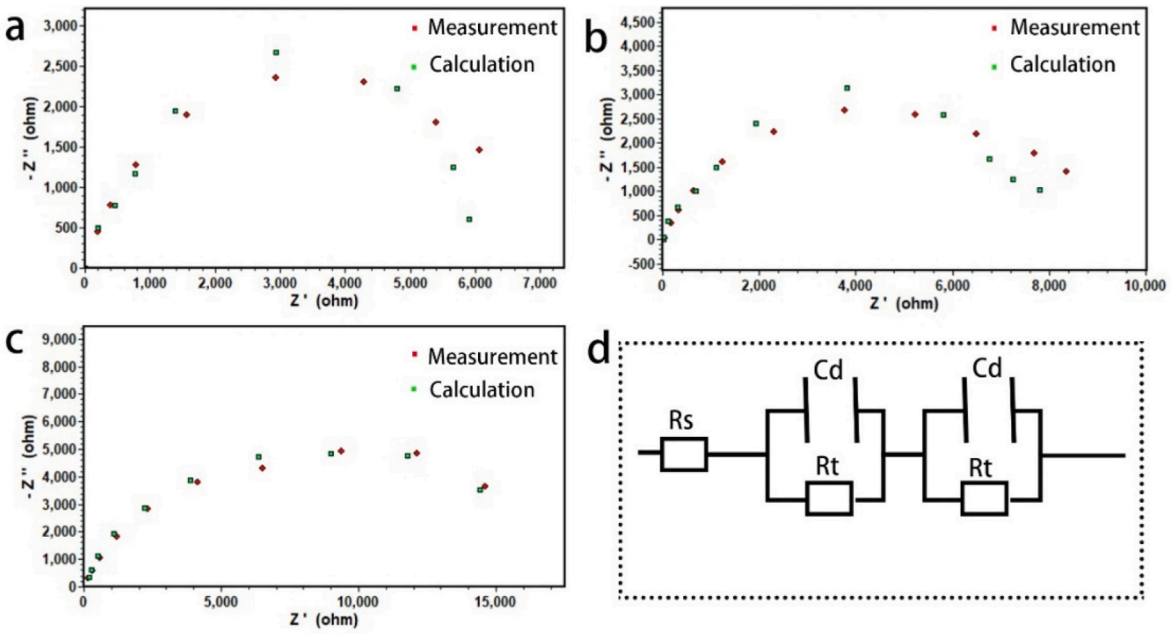

Fig. 10. Nyquist plots of the three parts (a: part 1, b: part 2, c: part 3) and equivalent circuit (d).

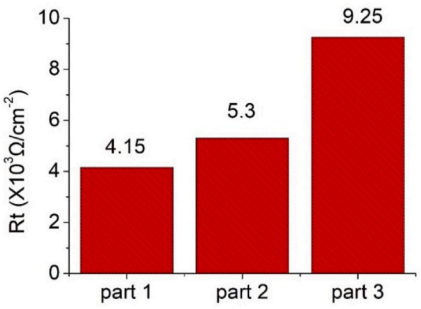

Fig. 11. R_t of the parts.

(shown by the black dashed rectangle). After tensile test, they have a gradient hierarchical structures trend are obtained that varies from a random large columnar crystals state to a gradually refined fine-grain state along the radial direction. Fig. 7b, d and f exhibit the grain size distribution. According to the column map, a gradient effect is clearly presented. After comparison, it is found that the number of grains (less than 50 μm) of sample 1 is significantly higher than that of sample 2 and sample 3. This also verifies that with the increase of copper content, the grains produced by WAAM can be refined.

Since both Cu and Ni are face-centered cubic (FCC) lattices. The twinning critical shear stress of FCC metal is much larger than the slip critical shear stress, so twinning deformation generally does not occur, and no deformation twinning is found in the deformed structure, so the plastic deformation of the material is mainly accomplished by slip, and the higher the SF, the greater the probability of the slip system being activated. In other words, a deformation mechanism with a higher SF is more likely to be activated and vice versa [27]. In addition, when there is a certain high SF in the alloy, the degree of difficulty of the slip system required to initiate deformation in a certain direction during plastic deformation is different, resulting in differences in strength and plasticity, and this difference increases with the increase of SF. Open the corresponding source file in the Tango program of the Channel 5 software. In order to improve the accuracy of the data, first remove the mislabeled points, and then find the corresponding SF map for input. Since there are three sets of SF maps with different parts, for the convenience of comparison, we export the data of the three parts of SF maps in Tex. format. Then use Origin software to map. As Fig. 8 shows that the SF of sample 3 is the highest, followed by sample 2, and sample 1 is the lowest. Therefore, sample 3 slips most easily when tensile stress is applied. This is further confirmed in conjunction with the SF and tensile specimen results for the samples in Fig. 8.

3.4. Corrosion behavior

The corrosion potential (E_{corr}) usually indicates the size of the thermodynamic corrosion tendency, and the larger the value of E_{corr} is, the better the corrosion resistance. The breakdown potential (E_{pit}) reflects

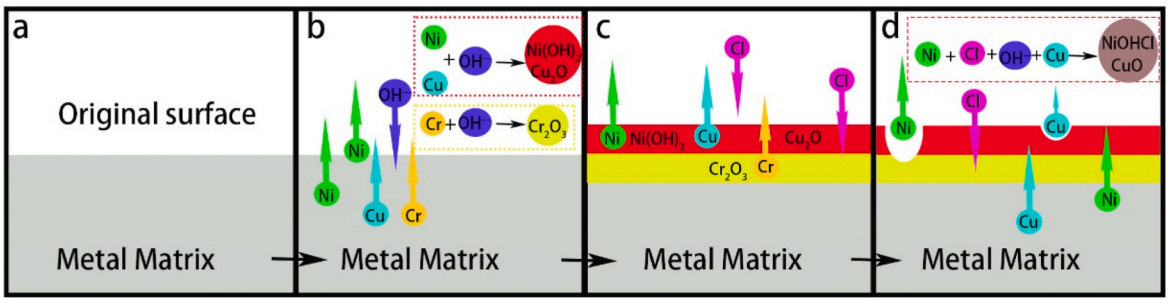

Fig. 12. Schematic of the corrosion mechanism.

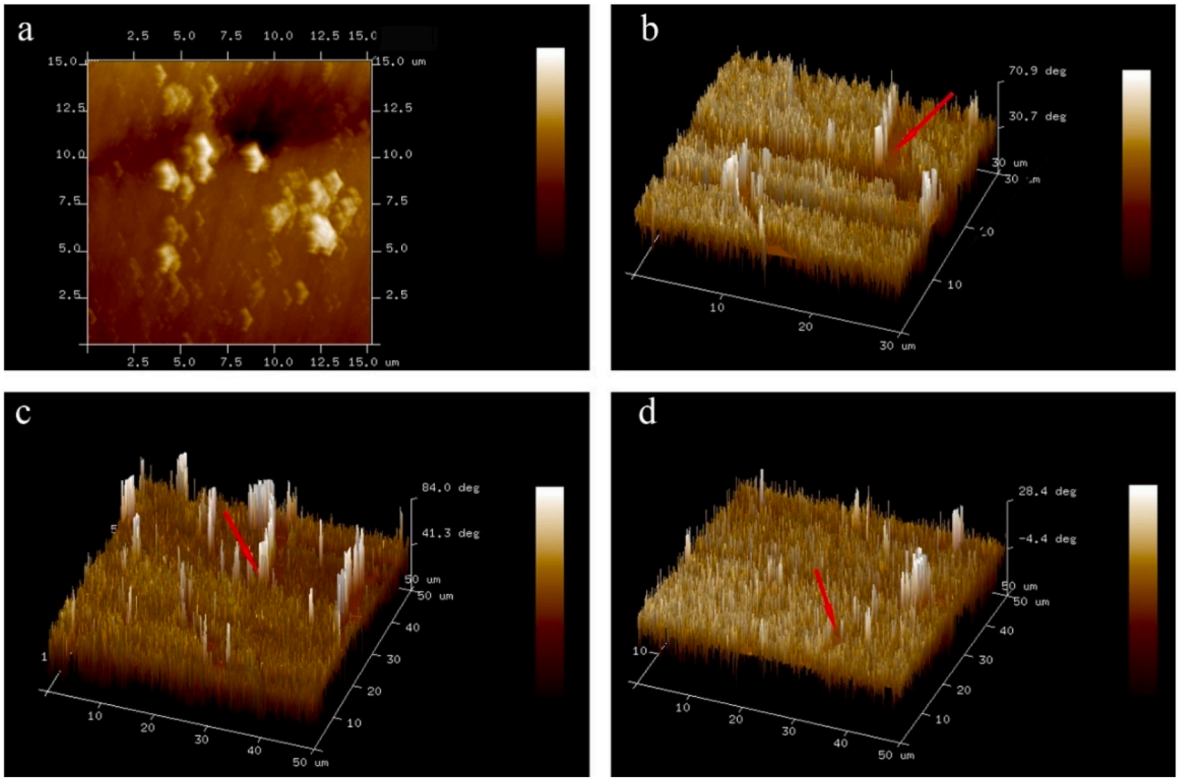

Fig. 13. AFM images of the surface of part 1(a, d), part 2 (c) and part 3(b).

the stability of the passivation film formed on the surface of a material. The larger the value of E_{pit} is, the more stable the passivation film formed and the less likely it is to be damaged (corroded). The corrosion current density (I_{corr}) represents the current density reflected by anode dissolution after the material is passivated. Bakkar [28] found that the smaller the value of I_{corr} is, the greater the corrosion resistance. Fig. 9 shows the polarization curves of part 1, part 2 and part 3 in a 3.5% NaCl solution. The results showed that the polarization curves of these specimens were slightly shifted in the noble direction. In the marked region (yellow ellipse mark) of the polarization curves, I_{corr} hardly changes with the increase in potential, that is, in the passivation zone. This is due to the reaction that forms Ni on the surface of the alloy. Sun [29] also found that the $(OH)_2$/NiO layer and internal Cr_2O_3 layer form a stable oxide film. When the potential value continues to increase to a certain value, I_{corr} increases again, accelerating the corrosion of the alloy electrode. This process usually leads to pitting corrosion on the electrode surface. Through the research of Gholami [30], the potential value at this time is defined as E_{pit}.

The corrosion parameters (E_{corr}, E_{pit} and I_{corr}) of the three parts are given in Table 4. The highest E_{corr} value is shown by part 3, which is −198 mV. The smallest E_{corr} value is shown by part 1, which is −300 mV. The same trend is seen for the E_{pit} value. The highest E_{pit} value is shown by part 3, which is 285 mV. The smallest E_{pit} value is shown by part 1, which is 218 mV. The smallest I_{corr} value is shown by part 3, which is 0.049 μA/cm^2. The highest I_{corr} value is shown by part 1, which is 0.124 μA/cm^2. It can be seen from the above data analysis that part 3 exhibits the highest corrosion resistance. The corrosion resistance of part 2 is second only to that of part 3. The corrosion resistance of part 1 is the lowest. Additionally, the corrosion results of WAAM Inconel 625 Ni–Cu functionally graded materials are better than those of the wrought Inconel 625 samples and laser cladding Inconel 625 samples (listed in Table 4), which demonstrates that the WAAM Inconel 625 Ni–Cu functionally graded materials have excellent corrosion resistance.

Fig. 10 shows the Nyquist and equivalent circuits of the three parts. The fitting results and the actual errors are less than 10%, so the test result is reliable. The three sets of Nyquist diagrams are all composed of a single capacitive reactance arc, and there is no Warburg impedance. Therefore, the electrochemical corrosion test used in this work is completely electrochemically controlled, and the diffusion resistance is almost negligible. The capacitive reactance radius increases from part 1 to part 3, which indicates that the corrosion resistance from part 3 to part 1 is reduced. The equivalent circuit model is R(CR)(CR). This model shows that the electrolyte-solution uniformly seeps into the surface layer of the Ni–Cu alloy. R_s is the solution resistance, and R_t is the charge transfer resistance of the test surfaces, which represents the difficulty for the charge to pass through the two-phase interface between the electrode and the electrolyte solution during the electrode reaction. Lu [33] found that the larger the value of R_t is, the more difficult the corrosion reaction is, and the better the corrosion resistance of the material.

As shown in Fig. 11, the R_t of part 3 is the largest compared with part 2 and part 1. The R_t of part 1 is the smallest, which indicates that the corrosion resistance of part 3 is the best, followed by part 2, and the corrosion resistance of part 1 is the worst.

This series-connected R(CR)(CR) equivalent model shows that during the electrochemical corrosion process, two layers of oxide films are formed on the surface of the alloy. The outer layer is a Cu_2O/$Ni(OH)_2$/NiO film, and the inner layer is a Cr_2O_3 film. Wang [34] also found a similar protective layer when he was studying nickel-based alloys. A schematic of the corrosion mechanism is shown in Fig. 12. When the Inconel 625 Ni–Cu functionally graded materials are corroded, first, a protective passivation film forms on the surface of the alloy. The protective film has two layers. The outer layer of the protective film is Ni $(OH)_2$/NiO and Cu_2O, and the inner layer of the protective film is Cr_2O_3, followed by the adsorption and erosion of corrosive ions such as Cl-, and finally the thinning of the protective film and the generation of cracks/defects.

As the diffusivity of Cr in the oxide film was much smaller than that of Cu and Ni, the stable film was a duplex of an inner Cr-rich layer and an outer Cu/Ni-rich layer [35,36]. Reaction (1) is the most important cathodic depolarization process in the system, and reaction (2) reflects

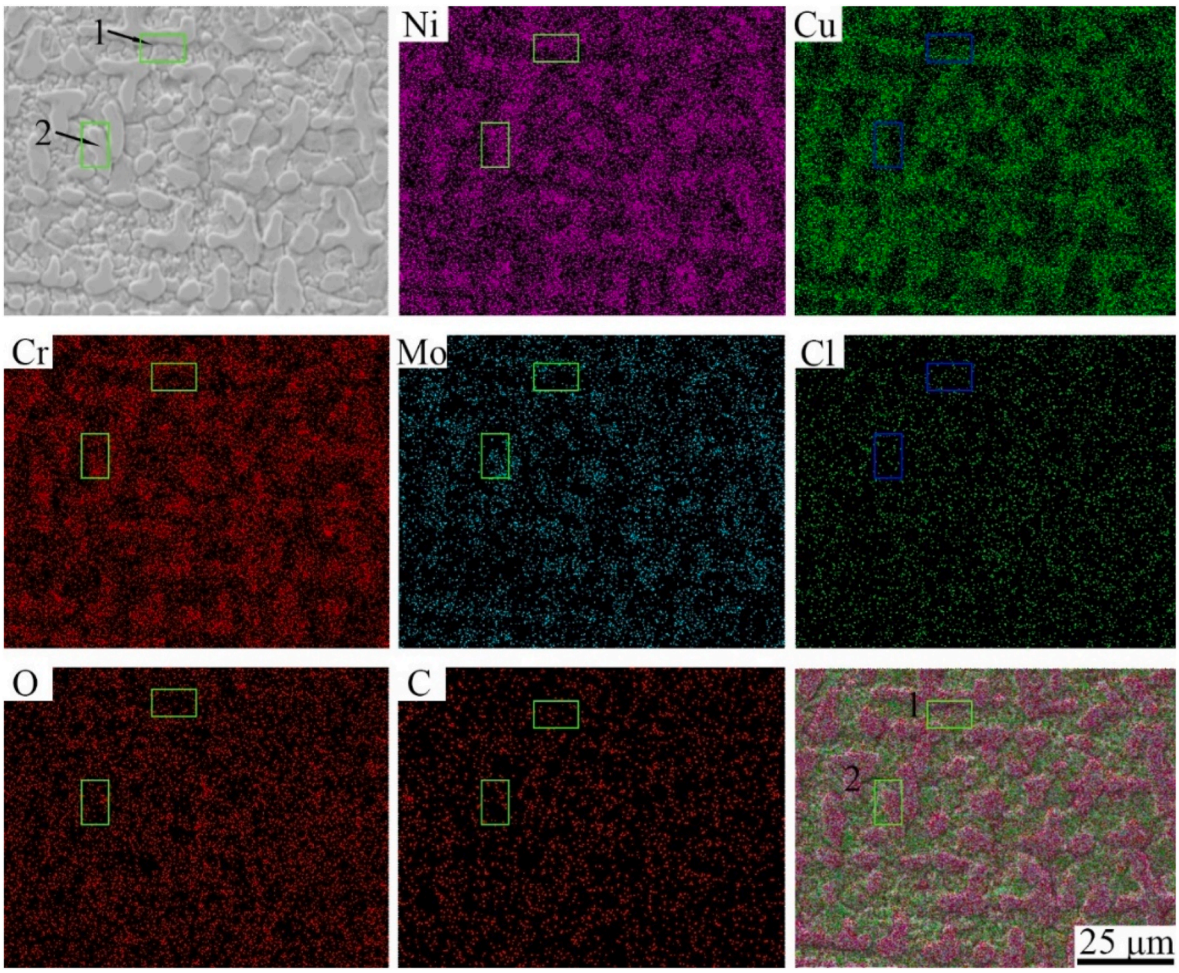

Fig. 14. SEM micrographs of corrosion on part 1.

that Cl^- promotes the anodic reaction. Reactions (3–7) reflect the establishment of a protective film. The existence of reaction (8) will make the Cu_2O protective film thinner and produce cracks/defects, resulting in a decrease in its protective performance.

$$O_2 + 2H_2O + 4e^- \rightarrow 4OH^- \quad (1)$$

$$Cu + 2Cl^- \rightarrow CuCl^- + e^- \quad (2)$$

$$2CuCl^- + 2OH^- \rightarrow Cu_2O + H_2O + 4Cl^- \quad (3)$$

$$Ni^{2+} + 2H_2O \leftrightarrow Ni(OH)_2 + 2H^+ \quad (4)$$

$$Cr^{3+} + 3H_2O \leftrightarrow Cr(OH)_3 + 3H^+ \quad (5)$$

$$Ni(OH)_2 \leftrightarrow NiO + H_2O \quad (6)$$

$$Cr(OH)_3 + Cr \rightarrow Cr_2O_3 + 3H^+ + 3e^- \quad (7)$$

$$Cu_2O + OH^- \rightarrow 2CuO + H_2O + 2e^- \quad (8)$$

In the atomic force microscopy (AFM) image of part 1 (Fig. 13a), it is clear that there are chains of pits (black) and chains of relief islands (white). These results indicate the pitting corrosion phenomenon. Generally, the pitting mechanism is related to the properties of the surface or matrix. It can be seen from the above analysis that as the content of Cu increases and the content of Cr decreases, the sample exhibits lower corrosion resistance. Yasakau [37] also showed that the addition of a low quantity of Cr improved corrosion resistance. From this, it is concluded that the more Cr there is, the stronger the resistance to pitting corrosion. It can form a smooth and compact layer/film on the sample, which forms dense contact for efficient charge migration and reduces recombination losses. This conclusion was confirmed by the reduction in the root mean square roughness value (R_q) from 12.8 nm (part 3) to 10.7 nm (part 2) and to 8.63 nm (part 1). From Fig. 13b-d, it can also be seen that the number and size of pits also decrease. These pits are mainly the result of severe corrosion. When corrosion starts, pitting occurs. As the concentration of Cl^- ions increases, the corrosion spreads to the surrounding surface and becomes localized corrosion, finally making the size of the pits larger.

The surface morphology of the electrochemically corroded part 1 sample was analyzed by scanning electron microscopy and is shown in Fig. 14. There were no serious corrosion marks on the surface of the sample. There were corrosion cracks at the grain boundaries (mark 1), and corrosion cracks (mark 2) also appeared inside individual grains. It can be seen from the element distribution that Cl is distributed in cracks and grain boundaries. Compared with grain boundaries, Mo and Cr, which are anti-corrosion elements, are significantly less abundant at the grain boundaries, while there are more oxides and carbides at the grain boundaries (carbide oxides are generally corrosion products). Therefore, corrosion starts from the grain boundaries and extends to the adjacent areas through the grain boundaries. There is another reason for corrosion starting from the grain boundaries, which is related to the characteristics of the grain boundaries. The grain boundary is the bonding interface between two different orientations of grains. Deacon [38] found that the electrode potential and the degree of electrochemical reaction in the grain boundary and the crystal are different, and the chemical stability of the grain boundary is poor, which makes the grain boundary undergo easier corrosion.

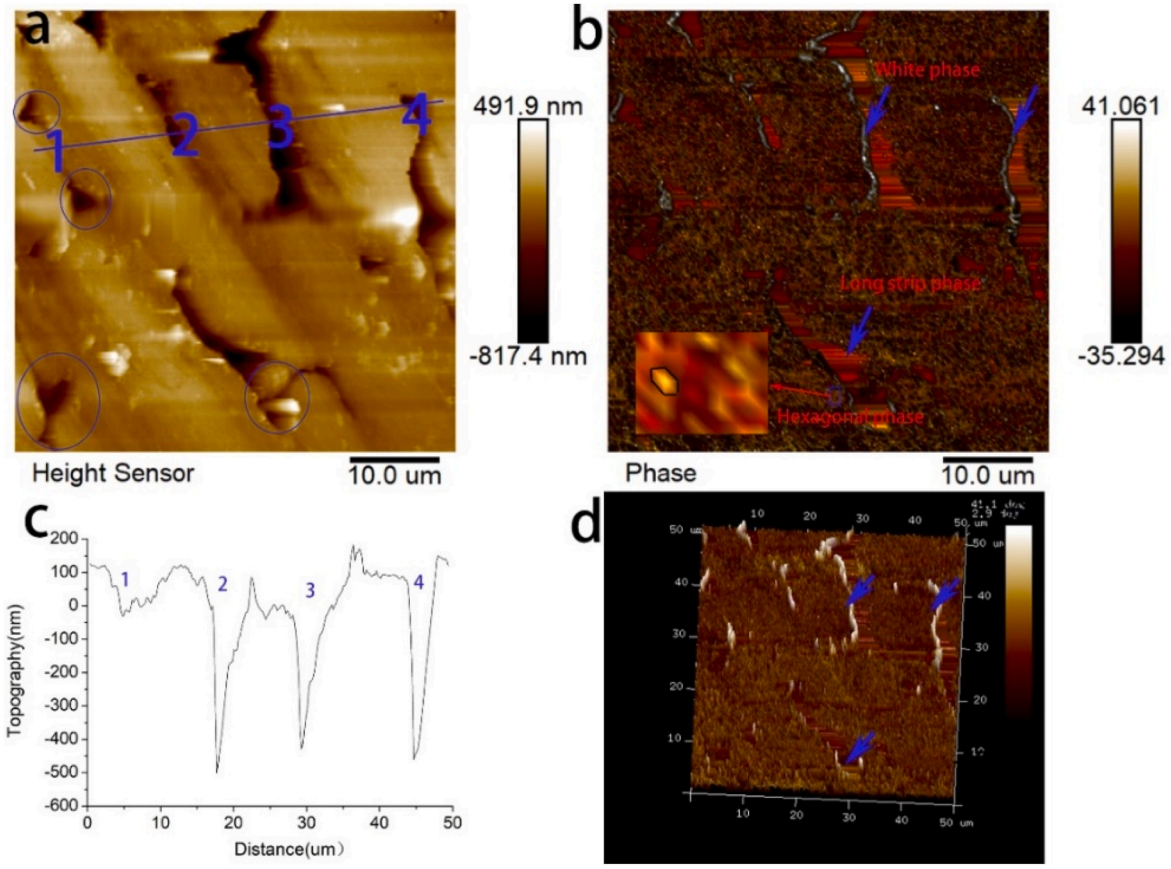

Fig. 15. Topography image (a) and phase image (b) of part 1, three dimensional images of phase (c) and the line profile (d).

To further analyze the corrosion phenomenon, topographic images and phase images were obtained by using conventional tapping mode AFM. It can be clearly seen from the phase Fig. 15 that the small white islands are regularly distributed on the surface. There were different phases (long strip phase and hexagonal phase) on both sides of the white islands. These different phases exhibited different corrosion behaviors. Serious corrosion occurred at the long strip phase, while the hexagonal phase was not corroded, mainly due to the formation of many micro galvanic cells during corrosion. Fig. 15a shows that the hexagonal phase is distributed in the crystal grains, while the elongated phase is mainly distributed at the grain boundaries. Through the above analysis of the element distribution, there is a lack of corrosion-resistant Cr and Ni elements at the grain boundaries, and the crystals are rich in Cr and Ni elements. Therefore, the hexagonal phase quickly formed a stable, dense protective film in a short period of time. In Fig. 15a, some deep corrosion grooves are distributed at the grain boundaries, and some corrosion pits can also be observed (marked circle). Through the analysis of the topography of the grains and grain boundaries, it can be seen that the region far from the grain boundaries is smooth, unlike the region near the grain boundaries. This shows that the protective film is unstable at the grain boundaries. Far from the grain boundary, the corrosion product film was uniform, which hindered the transport of ions and charges and improved the corrosion resistance of the Inconel 625 Ni–Cu functionally graded materials.

4. Conclusions

In this paper, based on preliminary experiments of additive manufacturing of dissimilar materials, one without a discrete interface, a wall of Inconel 625 Ni–Cu functionally graded materials was successfully deposited. This was conducted by optimizing the processing parameters and varying the feeding ratio of ERNiCrMo-3 wire and 99.9% Cu wire into a molten pool during the additive manufacturing process. The microstructure, mechanical properties and corrosion properties of the deposited alloy were investigated. The following conclusions can be drawn from the present work.

1) Inconel 625 Ni–Cu functionally graded materials can be obtained through plasma arc additive manufacturing. The microstructure and hardness change smoothly with composition changes.
2) Since the addition of Cu can increase the compositional supercooling zone, it can improve the defects inherent in the formation of columnar crystals in additive manufacturing. As a result, the WAAM Inconel 625 Ni–Cu functionally graded materials have excellent corrosion resistance, high strength and ductility. The performance is better than that of the Inconel 625 sample prepared by sand casting.
3) The R(CR)(CR) equivalent model shows that during the electrochemical corrosion process, two layers of oxide films are formed on the surface of the alloy: the outer layer is the $Cu_2O/Ni(OH)_2/NiO$ film, and the inner layer is the Cr_2O_3 film. The more severe the corrosion, the higher the surface roughness. With an increase in the content of Cu, the corrosion resistance decreases, the reduction in the root mean square roughness value (Rq) from 12.8 nm (part 3) to 10.7 nm (part 2) and to 8.63 nm (part 1).

CRediT authorship contribution statement

Yanhu Wang: Conceptualization, Investigation, Methodology, Writing – original draft, Funding acquisition. **Sergey Konovalov:** Supervision, Writing – review & editing. **Xizhang Chen:** Supervision, Funding acquisition. **R. Arvind Singh:** Writing – review & editing. **S. Jayalakshmi:** Writing – review & editing.

Declaration of competing interest

The authors declare that they have no known competing financial interests or personal relationships that could have appeared to influence the work reported in this paper.

Data availability

Data will be made available on request.

Acknowledgements

This work was sponsored by the National Natural Science Foundation of China under the Grant No. 51975419 and Foreign Experts Bureau Project of China under Grant No. QN20200116001, No. G2021016026L and No. G2021016026L.

References

[1] N. Noda, Thermal stresses in functionally graded materials, J. Therm. Stresses 22 (1999) 477–512, https://doi.org/10.1080/014957399280841.
[2] A.R. Studart, Biological and bioinspired composites with spatially tunable heterogeneous architectures, Adv. Funct. Mater. 23 (2013) 4423–4436, https://doi.org/10.1002/adfm.201300340.
[3] M.A. Meyers, J. McKittrick, P.Y. Chen, Structural biological materials: critical mechanics-materials connections, Science 339 (2013) 773–779, https://doi.org/10.1126/science.1220854.
[4] P.Y. Chen, J. McKittrick, M.A. Meyers, Biological materials: functional adaptations and bioinspired designs, Prog. Mater. Sci. 57 (2012), 16007, https://doi.org/10.1016/j.pmatsci.2012.03.001.
[5] A.R. Studart, Additive manufacturing of biologically-inspired materials, Chem. Soc. Rev. 45 (2016) 359–376, https://doi.org/10.1039/c5cs00836k.
[6] C. Zhang, F. Chen, Z. Huang, M. Jia, G. Chen, Y. Ye, Y. Lin, W. Liu, B. Chen, Q. Shen, L. Zhang, E.J. Lavernia, Additive manufacturing of functionally graded materials: a review, Mater. Sci. Eng. 764 (2019), 138209, https://doi.org/10.1016/j.msea.2019.138209.
[7] E. Müller, Č. Drašar, J. Schilz, W.A. Kaysser, Functionally graded materials for sensor and energy applications, Mater. Sci. Eng. 362 (2003) 17–39, https://doi.org/10.1016/S0921-5093(03)00581-1.
[8] B. Zhang, P. Jaiswal, R. Rai, S. Nelaturi, Additive manufacturing of functionally graded material objects: a review, J. Comput. Inf. Sci. Eng. 18 (2018), 41002, https://doi.org/10.1115/1.4039683.
[9] J.F. Groves, H.N.G. Wadley, Functionally graded materials synthesis via low vacuum directed vapor deposition, Compos. B Eng. 28 (1997) 57–69, https://doi.org/10.1016/s1359-8368(96)00023-6.
[10] R. Singh, V. Bhavar, P. Kattire, S. Thakare, S. Patil, R.K.P. Singh, A review on functionally gradient materials (FGMs) and their applications, in: IOP Conference Series: Materials Science and Engineering, 2017, 12021, https://doi.org/10.1088/1757-899X/229/1/012021.
[11] G. Udupa, S.S. Rao, K.V. Gangadharan, Functionally graded composite materials: an overview, Proced. Mater. Sci. 5 (2014) 1291–1299, https://doi.org/10.1016/j.mspro.2014.07.442.
[12] M. Naebe, K. Shirvanimoghaddam, Functionally graded materials: a review of fabrication and properties, Appl. Mater. Today 5 (2016) 223–245, https://doi.org/10.1016/j.apmt.2016.10.001.
[13] L. Yan, Y. Chen, F. Liou, Additive manufacturing of functionally graded metallic materials using laser metal deposition, Addit. Manuf. 31 (2020), 100901, https://doi.org/10.1016/j.addma.2019.100901.
[14] W.B. James, Powder metallurgy methods and applications, in: Powder Metallurgy, ASM International, 2018, pp. 9–19, https://doi.org/10.31399/asm.hb.v07.a0006022.
[15] R.M. Mahamood, E.T. Akinlabi, M. Shukla, S. Pityana, Functionally graded material: an overview, in: Proceedings of the World Congress on Engineering, Newswood Limited, 2012, pp. 1593–1597.
[16] P. Muller, J.Y. Hascoet, P. Mognol, Toolpaths for additive manufacturing of functionally graded materials (FGM) parts, Rapid Prototyp. J. 20 (2014) 309–314, https://doi.org/10.1108/RPJ-01-2013-0011.
[17] A. Safarzade, M. Sharifitabar, M. Shafiee Afarani, Effects of heat treatment on microstructure and mechanical properties of Inconel 625 alloy fabricated by wire arc additive manufacturing process, Transact. Nonferrous Met. Soc. China (Eng. Ed. 30 (2020) 3016–3030, https://doi.org/10.1016/S1003-6326(20)65439-5.
[18] J.F. Wang, Q.J. Sun, H. Wang, J.P. Liu, J.C. Feng, Effect of location on microstructure and mechanical properties of additive layer manufactured Inconel 625 using gas tungsten arc welding, Mater. Sci. Eng. 676 (2016) 395–405, https://doi.org/10.1016/j.msea.2016.09.015.
[19] Y. Wang, S. Konovalov, X. Chen, A.S. Ramachandra, J. Subramanian, Influence of silicon and magnesium on the mechanical properties of additive manufactured Cu-Al alloy, 3D Print. Addit. Manuf. 8 (2021) 331–339, https://doi.org/10.1089/3dp.2020.0321.
[20] Y. Wang, X. Chen, S. Konovalov, C. Su, A.N. Siddiquee, N. Gangil, In-situ wire-feed additive manufacturing of Cu-Al alloy by addition of silicon, Appl. Surf. Sci. 487 (2019) 1366–1375, https://doi.org/10.1016/j.apsusc.2019.05.068.
[21] D.H. Stjohn, M. Qian, M.A. Easton, P. Cao, The Interdependence Theory: the relationship between grain formation and nucleant selection, Acta Mater. 59 (2011) 4907–4921, https://doi.org/10.1016/j.actamat.2011.04.035.
[22] C. Guo, M. Ying, H. Dang, R. Hu, F. Chen, Microstructural and intergranular corrosion properties of Inconel 625 superalloys fabricated using wire arc additive manufacturing, Mater. Res. Express 8 (2021), 035103, https://doi.org/10.1088/2053-1591/abe977.
[23] W.X. Sun Wenbo, Junsong Jin, A hardness prediction model considering grain size effect for ferrite steel, J. Netshape Form. Eng. 7 (2015) 52–57, https://doi.org/10.3969/j.issn.1674-6457.2015.03.101.
[24] B. AlMangour, D. Grzesiak, J.M. Yang, In-situ formation of novel TiC-particle-reinforced 316L stainless steel bulk-form composites by selective laser melting, J. Alloys Compd. 706 (2017) 409–418, https://doi.org/10.1016/j.jallcom.2017.01.149.
[25] M. Swamy, P. Laxminarayana, A.H.V. Pavan, M.C. Antony Harison, G. Jayaraman, K. Singh, Microstructural characterization and mechanical properties of sand cast and investment cast alloy 625 for HP/IP casing applications for advanced fossil fired power plants, in: Materials Today: Proceedings, 2018, pp. 27118–27122, https://doi.org/10.1016/j.matpr.2018.09.019.
[26] W. Yangfan, C. Xizhang, S. Chuanchu, Microstructure and mechanical properties of Inconel 625 fabricated by wire-arc additive manufacturing, Surf. Coating. Technol. 374 (2019) 116–123, https://doi.org/10.1016/j.surfcoat.2019.05.079.
[27] Z.R. Zeng, M.Z. Bian, S.W. Xu, C.H.J. Davies, N. Birbilis, J.F. Nie, Effects of dilute additions of Zn and Ca on ductility of magnesium alloy sheet, Mater. Sci. Eng. 674 (2016) 459–471, https://doi.org/10.1016/j.msea.2016.07.049.
[28] A. Bakkar, M.M.Z. Ahmed, N.A. Alsaleh, M.M.E.S. Seleman, S. Ataya, Microstructure, wear, and corrosion characterization of high TiC content Inconel 625 matrix composites, J. Mater. Res. Technol. 8 (2019) 1102–1110, https://doi.org/10.1016/j.jmrt.2018.09.001.
[29] H. Sun, X. Wu, E.H. Han, Effects of temperature on the protective property, structure and composition of the oxide film on Alloy 625, Corrosion Sci. 51 (2009) 2565–2572, https://doi.org/10.1016/j.corsci.2009.06.043.
[30] M. Gholami, M. Hoseinpoor, M.H. Moayed, A statistical study on the effect of annealing temperature on pitting corrosion resistance of 2205 duplex stainless steel, Corrosion Sci. 94 (2015) 156–164, https://doi.org/10.1016/j.corsci.2015.01.054.
[31] J.M. Capus, Adv. powder metall. proces. Adv. Mater. Proces. 156 (1999) 33–36.
[32] T.E. Abioye, D.G. McCartney, A.T. Clare, Laser cladding of Inconel 625 wire for corrosion protection, J. Mater. Process. Technol. 217 (2015) 232–240, https://doi.org/10.1016/j.jmatprotec.2014.10.024.
[33] Y. Lu, J. Dong, W. Ke, Corrosion evolution of low alloy steel in deaerated bicarbonate solutions, J. Mater. Sci. Technol. 31 (2015) 1047–1058, https://doi.org/10.1016/j.jmst.2014.10.013.
[34] L. Wang, H. Li, Q. Liu, L. Xu, S. Lin, K. Zheng, Effect of sodium chloride on the electrochemical corrosion of Inconel 625 at high temperature and pressure, J. Alloys Compd. 703 (2017) 523–529, https://doi.org/10.1016/j.jallcom.2017.01.320.
[35] J. Buffle, Z. Zhang, K. Startchev, Metal flux and dynamic speciation at (Bio) interfaces. Part I: critical evaluation and compilation of physicochemical parameters for complexes with simple ligands and fulvic/humic substances, Environ. Sci. Technol. 41 (2007) 1–29, https://doi.org/10.1021/es070702p.
[36] X. Zhong, E.H. Han, X. Wu, Corrosion behavior of Alloy 690 in aerated supercritical water, Corrosion Sci. 66 (2013) 369–379, https://doi.org/10.1016/j.corsci.2012.10.001.
[37] K. Yasakau, Application of AFM-based techniques in studies of corrosion and corrosion inhibition of metallic alloys, Corros. Mater. Degrad. 1 (2020) 345–372, https://doi.org/10.3390/cmd1030017.
[38] R.M. Deacon, J.N. DuPont, A.R. Marder, High temperature corrosion resistance of candidate nickel-based weld overlay alloys in a low NOx environment, Mater. Sci. Eng. 460–461 (2007) 392–402, https://doi.org/10.1016/j.msea.2007.01.150.